metals

MDPI

Article

Study on the Morphology, Wear Resistance, and Corrosion Resistance of CuSn12 Alloys Subjected to Machine Hammer Peening

Ning Nie [1,2], Lu Yu [1], Shouwei Xu [1], Qiyuan Tian [1], Chenchen Ding [1], Lihong Su [2,*] and Hui Wang [1,3,*]

[1] School of Mechanical Engineering, Nantong University, Nantong 226019, China; nn835@uowmail.edu.au (N.N.); 2310110003@stmail.ntu.edu.cn (L.Y.); 2310110228@stmail.ntu.edu.cn (S.X.); 2310110359@stmail.ntu.edu.cn (Q.T.); 2210310005@stmail.ntu.edu.cn (C.D.)
[2] School of Mechanical, Materials, Mechatronic and Biomedical Engineering, University of Wollongong, Wollongong, NSW 2522, Australia
[3] Institute for Industrial Science, The University of Tokyo, Chiba 153-8505, Japan
* Correspondence: lihongsu@uow.edu.au (L.S.); hui_wang@metall.t.u-tokyo.ac.jp (H.W.)

Abstract: In this study, machine hammer peening (MHP) was employed to enhance the surface properties of CuSn12 alloys, and the effects of different impact energies on the surface morphology, mechanical properties, and electrochemical properties were systematically investigated. The results revealed that the surface morphology evolution after MHP treatment exhibited unique non-monotonic characteristics, which significantly differed from the surface effects of conventional shot peening technology. Microhardness tests indicated that the surface hardness increased by 40% to approximately 150 HV after treatment with 3.5 J impact energy. Friction and wear tests demonstrated that specimens treated with 2.7 J impact energy exhibited optimal wear resistance, with an 82.7% reduction in volume wear loss, and the wear mechanism transformed from composite wear to mild fatigue wear. Electrochemical performance tests showed that corrosion resistance continuously improved as the impact energy increased from 2.7 J to 3.5 J, primarily attributed to grain refinement and passive film formation; however, treatment with 1.7 J impact energy resulted in decreased corrosion resistance. The results demonstrate that optimizing MHP process parameters can significantly enhance the overall properties of CuSn12 alloys, providing a novel technical approach for the surface-strengthening of this alloy.

Keywords: machine hammer peening; CuSn12; topography; wear resistance; corrosion resistance

check for updates

Academic Editor: Roy Johnsen

Received: 4 February 2025
Revised: 7 April 2025
Accepted: 9 April 2025
Published: 16 April 2025

Citation: Nie, N.; Yu, L.; Xu, S.; Tian, Q.; Ding, C.; Su, L.; Wang, H. Study on the Morphology, Wear Resistance, and Corrosion Resistance of CuSn12 Alloys Subjected to Machine Hammer Peening. *Metals* **2025**, *15*, 444. https://doi.org/10.3390/met15040444

Copyright: © 2025 by the authors. Licensee MDPI, Basel, Switzerland. This article is an open access article distributed under the terms and conditions of the Creative Commons Attribution (CC BY) license (https://creativecommons.org/licenses/by/4.0/).

1. Introduction

Bronze is widely used in marine engineering, shipbuilding, and precision machinery due to its excellent wear resistance [1], good self-lubricating properties [2], and outstanding corrosion resistance [3]. Tin bronze finds extensive applications in critical tribological components, such as bushings and bearings and propellers and fittings, where they are subjected to aggressive corrosive environments [4,5]. These severe working conditions necessitate exceptional material performance characteristics, particularly in terms of tribological resistance, fatigue endurance, and corrosion resistance [6]. However, the intrinsic mechanical properties of bronze impose significant limitations on their permissible contact stress and load-bearing capacity, constraining its broader industrial applications [7,8].

Surface treatment methods, such as shot peening, laser shock peening, and water cavitation jet peening, are widely recognized for their effectiveness in improving the surface

strength [9–11], corrosion resistance [12,13], and fatigue life of materials [14]. The wear resistance of material is governed by multiple factors, including precipitate distribution, surface topography, microstructure, stress state, and lubrication conditions. Consequently, surface treatment processes influence wear behavior in complex ways. The enhancement of wear resistance typically results not from a single dominant factor but from the synergistic interaction of multiple mechanisms. Jia et al. [15] studied the dry sliding wear of shot peened medium manganese steel under different conditions and found that the wear resistance of hot-rolled steel after shot peening was improved through twin-mediated stress relaxation, while the wear resistance of solution-treated steel was deteriorated due to dislocation-induced cracking. Li et al. [16] developed a micro-laser shock peening technique for 9310 steel surface-strengthening. The results revealed a significant wear rate reduction attributed to the formation of dimpled structures and hardened layers. The dimpled structures enhanced surface roughness while reducing the effective contact area, whereas the hardened layer slowed the onset of wear behavior. Overall, surface treatment technologies can improve the wear resistance for most materials.

Surface treatments that enhance wear resistance may simultaneously affect the corrosion behavior of treated materials. The corrosion behavior of materials is mainly governed by their surface integrity characteristics, including microhardness, stress state, surface topography, and microstructure [17–20]. Surface treatment technologies inevitably introduce microstructure strengthening and stress strengthening, leading to an improvement in corrosion resistance. On the other hand, the increase in surface roughness may cause a deterioration in corrosion behavior. Wu et al. [21] investigated the influence of shot peening on the corrosion and wear resistance of 2205 duplex stainless steel. The results indicated that structural refinement provides diffusion channels to form a passive film that is relatively enriched with chromium and molybdenum and improves the surface hardness and wear resistance of the steel. However, the increase in roughness leads to fluctuations in the current density during anodic polarization, and a higher repassive current density destroys the surface integrity and accelerates wear loss of the steel.

The formation of a passive film is also a crucial factor in enhancing the corrosion resistance of alloys. Lv et al. [22] investigated the corrosion behavior of bronze alloys after shot peening. The results showed that the corrosion current density decreased after shot peening, primarily due to grain refinement and homogenization, which facilitated the rapid formation of a protective passive film. However, the impedance arc diameter of the shot-peened samples was smaller than that of the untreated samples. To resolve this contradictory conclusion, Niu and his group [23,24] studied the corrosion current density of materials after shot peening. They were the first to propose comparing corrosion resistance using new indicators, such as polarization current density, corrosion equivalent resistance, charge passing through the material, and material mass loss. In summary, the effect of surface treatment technologies on material corrosion behavior depends on a balance between these positive and negative factors.

Machine hammer peening (MHP) is an advanced surface treatment technique that induces refined microstructure and higher compressive residual stresses in deeper layers compared to conventional surface-strengthening methods. In this work, CuSn12, a tin bronze that exhibits superior mechanical properties and excellent corrosion resistance in marine engineering applications, was selected as the target material. This study aims to investigate the effects of MHP treatment on mechanical properties, surface integrity, wear resistance, and corrosion behavior of CuSn12, elucidate the underlying mechanisms, and thereby expand its potential industrial applications.

2. Material and Experiment

2.1. Material and MHP

In this study, CuSn12 was used as the raw material, and its chemical composition is detailed in Table 1. The data source is the manufacturer's material certificate. The initial specimens were obtained from rolled plates and processed by wire electrical discharge machining to dimensions of 100 × 100 × 3 mm^3 (Figure 1a). The specimens were first annealed at 500 °C for 2 h under vacuum conditions, followed by air cooling to room temperature.

Table 1. Chemical composition of CuSn12 in wt.%.

Elements (wt.%)	Ni	Pb	Sn	Zn	P	Al	Fe	Mn	Cu
CuSn12	0.5	0.15	11.5	0.1	0.05	0.005	0.05	0.05	Bal.

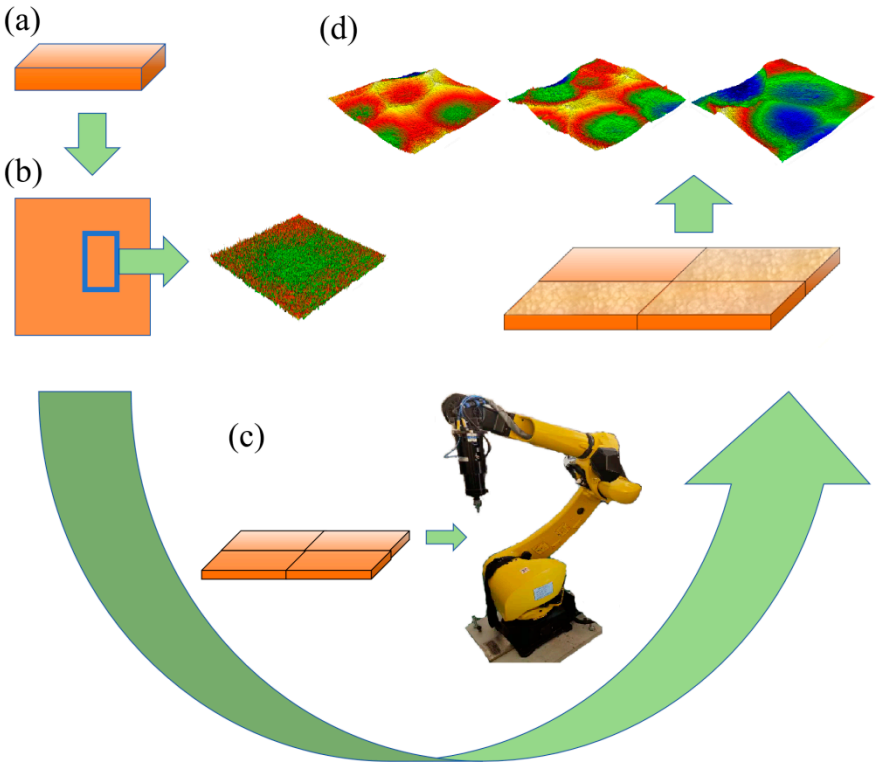

Figure 1. MHP surface-strengthening procedure (**a**) Untreated sample (**b**) Shooting laser confocal (**c**) Perform mechanical hammering (**d**) Laser confocal after hammering the sample.

A surface-strengthening treatment was performed using an electric impact hammer system with a hemispherical hammer head of 5 mm radius curvature for saturated hammering (Figure 1c). The impact energies were 1.7 J, 2.7 J, and 3.5 J, with the corresponding treated specimens designated as MHP-1.7, MHP-2.7, and MHP-3.5, respectively, while the untreated specimen was designated as unMHP.

2.2. Microhardness Measurement

For microhardness measurements, specimens were cut to dimensions of 20 × 20 × 3 mm^3. Subsequently, surface contaminants and residual cutting debris were removed using an ultrasonic cleaner and anhydrous ethanol. The Vickers hardness measurements were undertaken by a tester FM-810 (FUTURE TECH, Kanagawa, Japan) with an applied load of 1.962 N for a duration of 10 s. Measurements were performed on the rolling plane of the plate, namely the TD-ND plane. For depths within 500 μm, hardness values were measured

at 50 μm intervals; between 500 and 1000 μm, measurements were taken at 100 μm intervals; and from 1000 to 3000 μm, measurements were conducted at 200 μm intervals. To minimize error, surface hardness testing was repeated three times for each specimen, and the average values were recorded.

2.3. Surface Morphology Investigation

To investigate the effects of MHP surface treatment with different energies on the surface morphology of CuSn12, a high-resolution confocal microscope (μsurf mobile, NanoFocus, Oberhausen, Germany) was employed to observe and measure the surface morphology of MHP-treated and unMHP samples (Figure 1b,d). The three-dimensional morphology and roughness of these specimens were compared before and after surface treatment, and the influence of specimens subjected to different energies on surface morphology was analyzed. Furthermore, field emission scanning electron microscopy (SEM) (ZEISS Gemini SEM 300, ZEISS, Oberhausen, Germany) was utilized to observe and analyze the morphology of specimens after friction and wear testing, revealing the influence of different impact energies on friction and wear behavior.

2.4. Friction and Wear Testing

In this study, friction and wear testing was conducted using a multifunctional tribometer (MFT-5000, RTEC Instruments Inc., San Jose, CA, USA). The experiments employed a pin-on-flat reciprocating sliding contact method, with the pin made of SiC material. Prior to testing, specimen surfaces were cleaned to remove oil contamination and debris, followed by a drying treatment. The reciprocating friction tests were performed at 20 °C with a frequency of 1 Hz, an applied load of 50 N, and a test duration of 10 min, while the reciprocating displacement was 9 mm. Each test was repeated three times to obtain the average wear volume, and the friction coefficient curve corresponding to the test closest to the mean wear volume was selected. Subsequently, high-resolution confocal microscopy was employed to observe the 3D morphology of specimens and investigate the wear mechanisms.

2.5. Electrochemical Test

In this study, electrochemical methods were employed to evaluate the influence of MHP treatment on the corrosion resistance of CuSn12. An electrochemical workstation (CHI660, Chenhua Inc., Shanghai, China) was used to record the potentiodynamic polarization curves using a standard three-electrode configuration with a saturated calomel electrode (SCE) as the reference electrode. After the open circuit potential (OCP) reached stability, polarization tests were conducted within a potential range of −0.652 V to 0.35 V vs. SCE at a scan rate of 1 mV/s. Potentiostatic polarization tests were performed in 3.5 wt% NaCl solution. All tests were conducted at 20 °C. Three specimens under the same impact energy were tested three times to ensure result reliability.

3. Results and Discussion

3.1. Microhardness

Surface modification technologies can significantly enhance the surface hardness of specimens. Figure 2 demonstrated the microhardness distribution across the depth from the surface for specimens subjected to four different impact energies. The unMHP specimen exhibited Vickers hardness, fluctuating around 105 HV after annealing. Specimens subjected to MHP treatment demonstrated substantially elevated surface hardness values compared to the untreated control, with peak hardness values manifesting in the surface and subsurface regions. The microhardness profiles revealed a gradient distribution,

wherein hardness values systematically decrease with increasing depth from the surface. This decline continues until the hardness values ultimately converge to approximately 105 HV, corresponding to the baseline hardness observed in the untreated specimen. This convergence suggests that the plastic deformation induced by the impact treatment has a finite depth of influence, beyond which the material properties remain unaffected by the surface modification process.

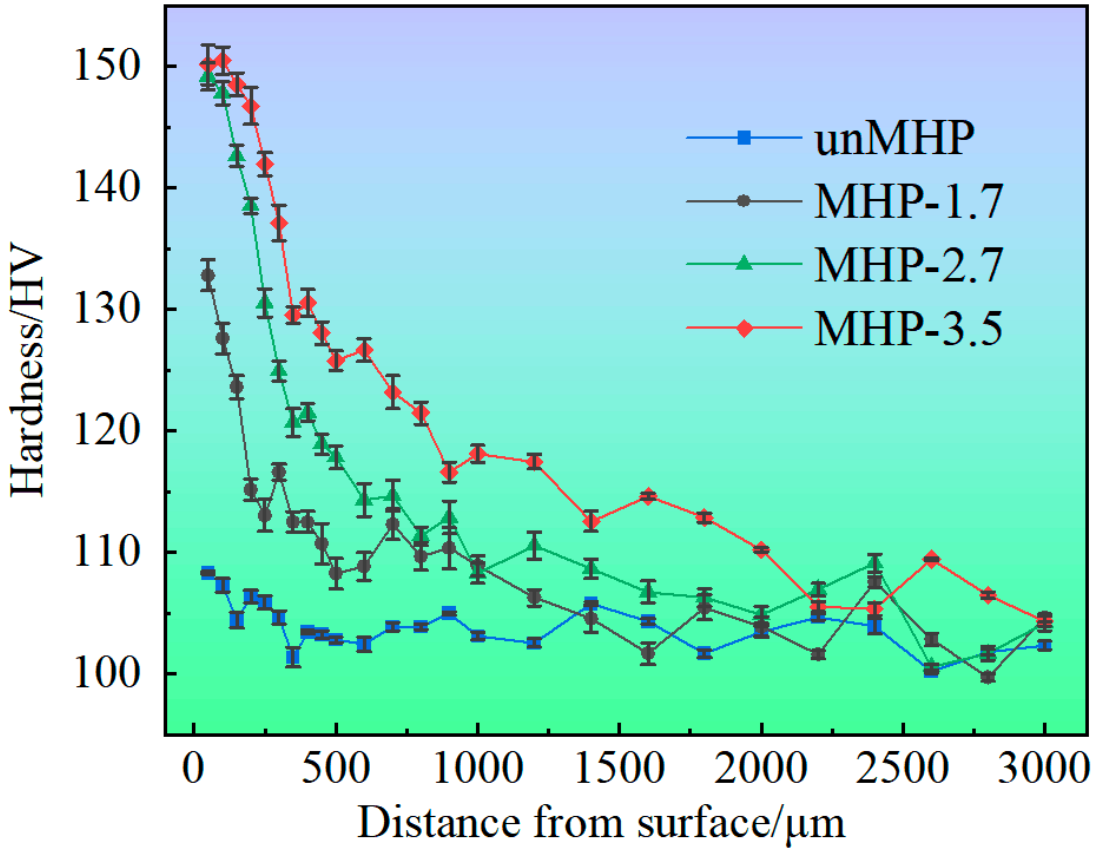

Figure 2. The microhardness distribution of untreated and treated samples.

MHP-3.5 exhibits the highest surface hardness at approximately 150 HV, representing an increase of about 40% compared to the unMHP specimen. MHP-2.7 exhibited surface and sub-surface hardnesses similar to MHP-3.5. The hardness values did not increase with rising impact energy, suggesting that the maximum hardening capacity of the MHP technique had been reached. Dislocation multiplication and annihilation achieved equilibrium in this area with peak dislocation density and minimum achievable grain size. At the same depth, MHP-1.7 exhibited the lowest hardness values compared to the other two impact specimens, indicating that higher impact energy produced greater plastic deformation at the surface, resulting in higher hardness. As specimen thickness increased, the hardness of all samples decreased dramatically, and the most dramatic decrease occurred within the first 500 μm.

Generally, the depth of the hardened layer correlates with impact energy [25,26]. MHP-1.7 showed a rapid decrease in hardness with increasing depth, approaching the level of the untreated specimen at 1400 μm, indicating a relatively shallow hardened layer. In contrast, MHP-3.5 maintained elevated hardness until approximately 2200 μm from the surface before declining to the hardness level of the unMHP specimen. MHP-2.7 exhibited intermediate characteristics, with a hardened layer depth of approximately 2000 μm.

Gomez et al. investigated the effect of MHP on the mechanical properties of high-strength structural steel S690 [27] and found that the surface microhardness reached a

peak hardness of about 350 HV, which was 40% higher than that of the untreated sample. Another study conducted by Curtat et al. revealed a significant increase in subsurface hardness for martensitic stainless steel treated with MHP, reaching a depth of at least 4 mm [28]. These studies indicate that, compared to other strengthening techniques, MHP demonstrates superior surface-strengthening capabilities. Tang et al. [25] reported that the laser shock strengthening of copper–tin alloy achieved an influence depth of approximately 0.35 mm, significantly less than the 2 mm depth achieved in our work. Similarly, Li et al. [26] employed ultrasonic surface rolling to enhance the surface properties of Cu-Cr alloy, achieving a maximum influence depth of approximately 0.4 mm. These comparative results highlight the distinct advantages and broad application prospects of MHP compared to similar technologies.

3.2. Surface Morphology

Figure 3 presents the 3D surface topography of the specimens under varying MHP treatment energies by confocal microscope images. The untreated specimen (Figure 3a) exhibits a relatively flat surface with minimal height variations, showing a maximum height difference of approximately 22 μm, indicative of the original machined surface condition. As shown in Figure 4, this conclusion can be evidenced by an average roughness (Ra) of 0.98 μm and an Rt value (maximum height difference) of 8.88 μm.

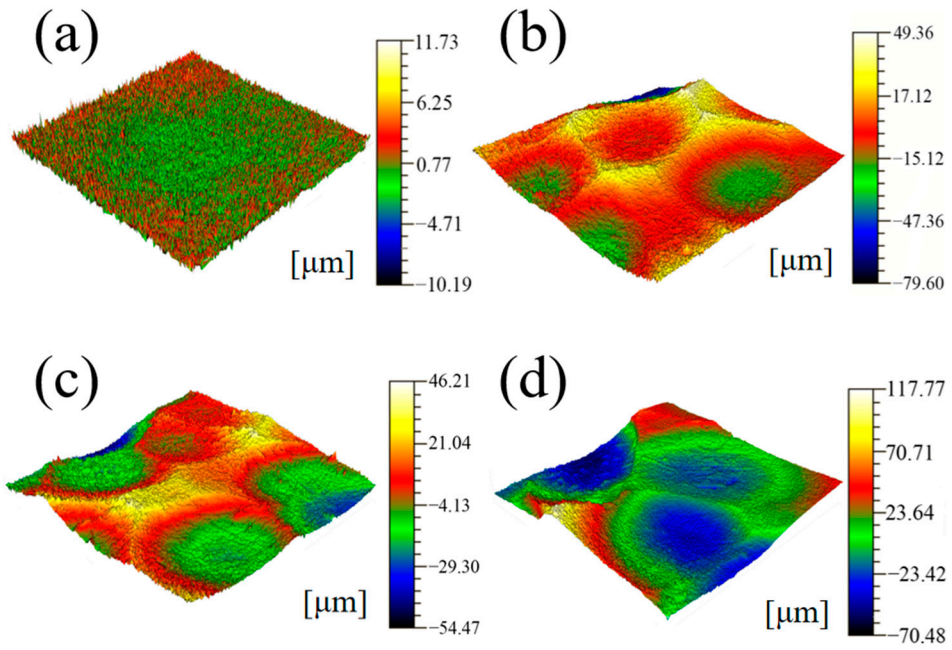

Figure 3. The confocal microscope image of (**a**) unMHP; (**b**) MHP-1.7; (**c**) MHP-2.7; and (**d**) MHP-3.5.

Upon MHP treatment, the surface underwent significant plastic deformation, characterized by distinctive crater-like features. Initially, the height differential increases with impact energy, as evidenced by surface deformation patterns exhibiting a height difference of approximately 180 μm at 1.7 J (Figure 3b), and the corresponding Ra and Rt values increased sharply to 4.69 and 36.01 μm, respectively, demonstrated the primary effects of the MHP process. However, when the impact energy increased to 2.7 J (Figure 3c), the surface morphology exhibited an unexpected reduction in height difference to around 100 μm, indicating a transition toward more uniform deformation patterns. This is accompanied by a decreased Ra value of 4.35 μm and a relatively stable Rt of 37.88 μm. It is important to note that while the height difference data were derived from individual confocal microscope images, the roughness values represented averages from five independent

measurements. The observed reduction in surface roughness suggests an optimization of surface integrity, attributed to higher dislocation density induced by increased plastic deformation; such microstructural evolution subsequently inhibits further plastic deformation processes through the strain-hardening mechanism. With a further increase in impact energy (3.5 J), the surface roughness demonstrates a renewed upward trend, with the height difference reaching approximately 188 μm. As illustrated in Figure 3d, the morphological features are characterized by more distinct valley/peak configurations.

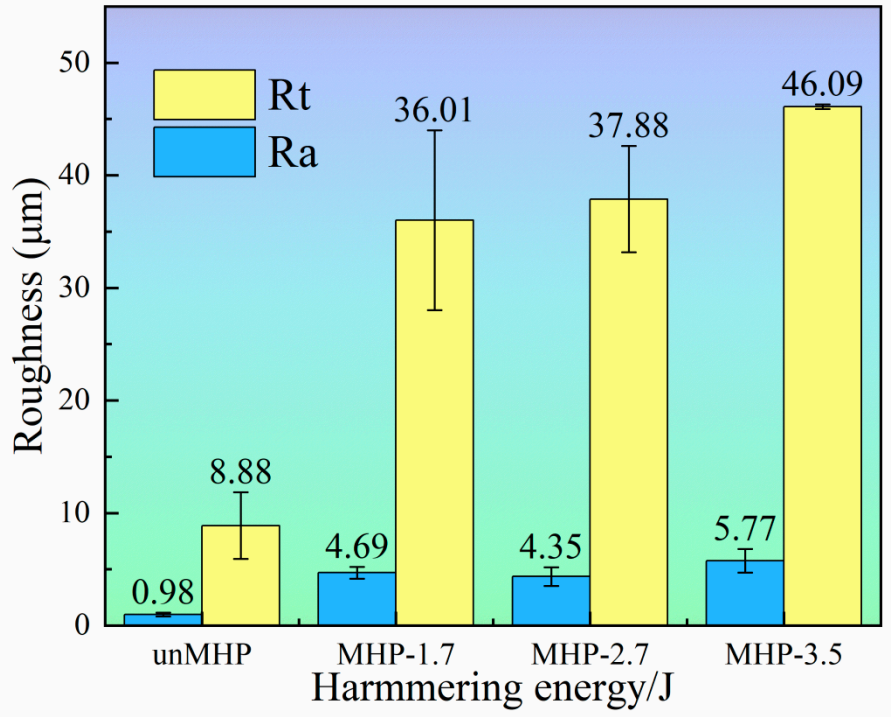

Figure 4. The roughness of different samples.

This non-linear trend differed from that observed in shot peening technology. Through simulation modeling, Liu et al. [29] investigated the relationship between surface roughness and processing parameters (shot peening pressure and shot size) for Al alloy. Their findings revealed a direct correlation between processing intensity and surface modification: both plastic deformation and surface roughness exhibited monotonic increases with elevated shot peening pressure and increased shot size.

Surface-strengthening technologies have been shown to enhance the corrosion resistance of materials [30–32]. For instance, the study by Kumar et al. [33] demonstrated that Ti-13Nb-13Zr alloys subjected to ultrasonic shot peening exhibited a reduced corrosion rate for all treated samples. This improvement in corrosion resistance is generally attributed to factors such as the formation of a grain-refined surface layer, changes in surface texture, and the introduction of compressive residual stresses. On the other hand, numerous studies have highlighted that surface roughness is a significant detrimental factor to corrosion resistance [34,35]. This correlation can be explained by two primary mechanisms: first, increased surface roughness from shot peening-like technologies enlarges the effective contact area between the material surface and the corrosive medium; second, the roughened surface provides additional active anodic sites, potentially accelerating the corrosion process.

In this study, the MHP-2.7 sample appeared to strike a balance between surface roughness and plastic deformation, characterized by uniform deformation patterns and moderate height differences. The surface topography at this energy level showed well-distributed

impact features without the excessive deformation at higher energies. The evolution of surface morphology demonstrated that the MHP process significantly influences the surface topography of CuSn12, with the treatment energy playing a crucial role in determining the final surface characteristics. The optimal energy level of 2.7 J achieved effective surface modification while maintaining controlled deformation patterns. However, the surface showed more pronounced deformation for MHP-3.5. The surface features became more irregular and deeper, indicating potential over-deformation. The depression patterns at this energy level were larger and more pronounced, with more distinct valleys and peaks.

3.3. Wear Behavior

The wear behavior of CuSn12 exhibits remarkable sensitivity to hammering energy, as evidenced in Figure 5. Quantitative analysis reveals that unMHP suffered the highest volumetric wear loss of 26.01 mm^3. Particularly, MHP-1.7 dramatically reduced wear volume to 9.32 mm^3, representing a substantial 64.2% improvement. This significant enhancement underscores the considerable potential of machine hammering processing for industrial applications requiring enhanced wear resistance.

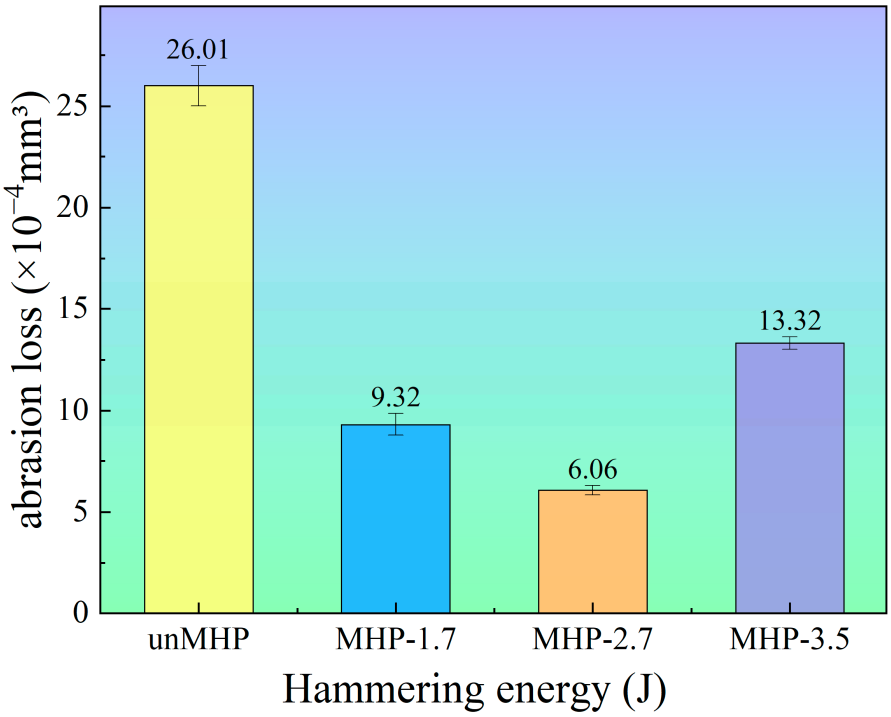

Figure 5. Volumetric wear loss after friction and wear under a load of 50 N.

When the hammering energy was increased for MHP-2.7, the wear volume further decreased to 6.06 mm^3, achieving an impressive 76.7% reduction compared to unMHP. This optimal performance of MHP-2.7 identifies it as a critical processing parameter for maximizing the wear resistance of CuSn12. However, MHP-3.5 led to a notable rebound in wear volume to 13.32 mm^3. Although this value remains lower than that of unMHP, it represents approximately a 120% increase compared to MHP-2.7. This elevation in wear volume can be attributed to increased surface roughness. Specifically, the more pronounced valley/peak topography may impede pin movement, resulting in elevated wear volume.

This non-linear wear behavior reveals the existence of an optimal window for hammering energy in relation to wear resistance. Moderate machine hammering effectively enhances wear resistance through multiple mechanisms, including surface hardening, optimization of residual stress distribution, and microstructural refinement [36]. However, excessive hammering energy can trigger detrimental effects, such as over-work hardening

of the surface layer and the formation of microcracks and other microstructural defects, ultimately compromising the material's wear resistance properties [37].

The evolution of friction behavior for CuSn12 subjected to varying hammering energies is comprehensively illustrated by the friction coefficient/time curves (Figure 6). Initially, all specimens underwent a brief running-in period characterized by rapid fluctuations in friction coefficients. Post running-in, unMHP exhibited a progressively increasing friction coefficient from approximately 0.3 to 0.55, accompanied by significant fluctuations throughout the testing period. These unstable tribological characteristics indicate poor surface properties and susceptibility to severe frictional damage in the untreated specimen.

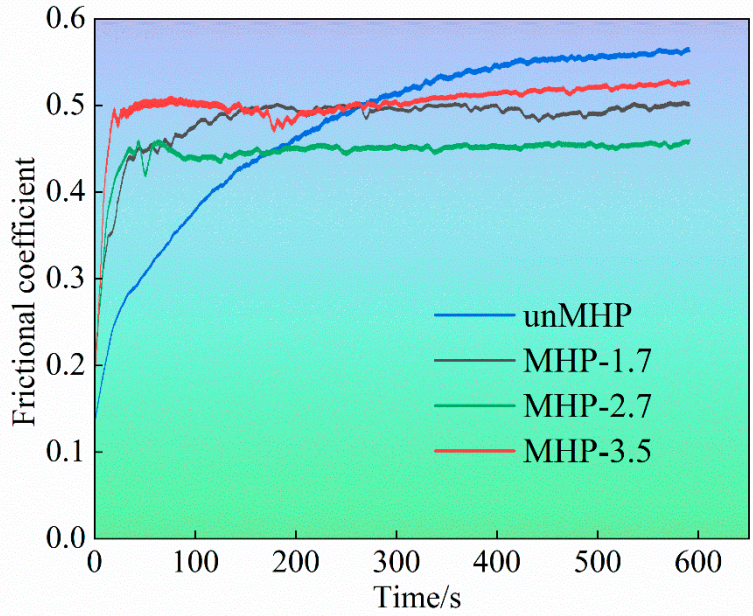

Figure 6. Friction coefficient/time graphs after friction and wear under a load of 50 N.

In contrast, MHP-1.7 demonstrated relatively stable friction behavior, with the friction coefficient oscillating around 0.5, suggesting that moderate machine hammering contributes to stabilizing tribological properties. Most notably, MHP-2.7 exhibited superior friction performance, characterized by both the lowest friction coefficient (approximately 0.45) and remarkable stability throughout the testing duration, displaying minimal curve fluctuations. These results indicate that the 2.7 J hammering energy induced optimal surface-strengthening effects, effectively suppressing severe frictional damage. However, when the hammering energy was further increased to 3.5 J, MHP-3.5 showed a slight elevation in friction coefficient, stabilizing at approximately 0.52, which correlates well with the previously observed wear volume trends.

The systematic evolution of friction behavior reveals the underlying mechanisms by which hammering energy modulates the tribological properties of the material. Moderate hammering treatment significantly enhances friction performance by optimizing surface hardness, residual stress state, and microstructural characteristics. Conversely, excessive hammering energy may compromise these beneficial effects, leading to performance degradation. These findings not only advance our understanding of the machine hammering strengthening mechanism but also provide robust experimental evidence for process parameter optimization [38,39].

A systematic investigation of the surface morphological characteristics modulated by hammering energy was conducted using three-dimensional topographical analysis (Figure 7). The results reveal distinctly different surface features after tribological test-

ing, reflecting significant variations in surface modification effectiveness across different treatment conditions.

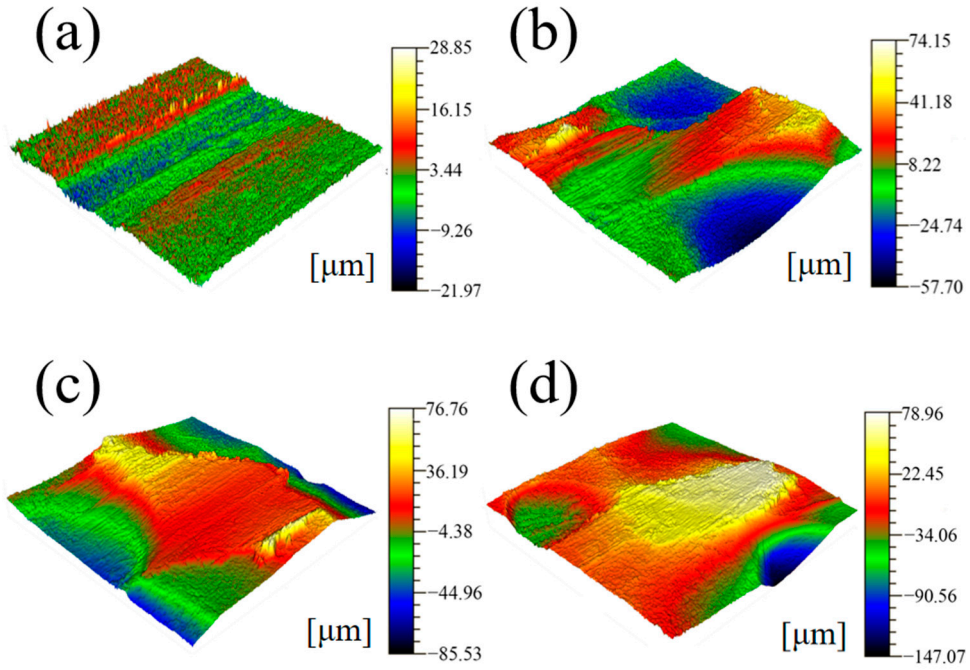

Figure 7. Three-dimensional morphology. (**a**) unMHP; (**b**) MHP-1.7; (**c**) MHP-2.7; and (**d**) MHP-3.5 of wear scars tested under a load of 50 N.

The surface of unMHP exhibited characteristic severe wear features, marked by intersecting deep plowing grooves and significant height variations. This severe surface damage pattern primarily resulted from intense plastic deformation and material delamination during friction. The relatively low surface hardness facilitated substantial debris formation, further intensifying the plowing effect, ultimately leading to significant surface deterioration. MHP-1.7 demonstrated notable surface quality enhancement: although groove structures remained observable, their distribution showed marked improvement. This enhancement can be attributed to moderate strain hardening induced by machine hammering, which improved both surface hardness and resistance to plastic deformation. Additionally, the hammering process likely induced beneficial compressive residual stresses, contributing to the suppression of microcrack initiation and propagation.

The MHP-2.7 achieved optimal morphological characteristics, featuring uniformly distributed wear tracks with moderate groove depths and excellent surface consistency. These superior surface properties likely stem from multiple factors: firstly, this energy level induced sufficient surface-strengthening without excessive deformation; secondly, the hammering process promoted grain refinement in the surface layer, resulting in a more compact microstructure; finally, this energy level achieved optimal residual stress distribution. However, MHP-3.5 exhibited significant morphological deterioration: despite maintaining relatively regular wear track arrangements, the surface height variations increased dramatically, with notable pit defects in localized regions. This performance degradation can be attributed to surface over-deformation and damage caused by excessive hammering energy, manifesting through (i) strain softening induced by excessive plastic deformation, (ii) microcrack formation and propagation due to high-energy impact, and (iii) potential disruption of the original microstructure, compromising overall material performance.

The three-dimensional topographical analysis clearly reveals the regulatory mechanism of hammering energy on CuSn12 surface characteristics: An optimal energy window

exists (2.7 J in this study) where maximum surface-strengthening effects can be achieved. These findings not only deepen our understanding of the MHP strengthening mechanism but also provide reliable experimental evidence for process parameter optimization. Future investigations could further establish comprehensive structure/property relationships by incorporating microstructural evolution and mechanical property characterization studies.

Systematic microscopic morphological analysis via SEM revealed the evolution of surface damage mechanisms and their underlying principles in CuSn12 specimens treated with varying machine hammering energies (Figure 8).

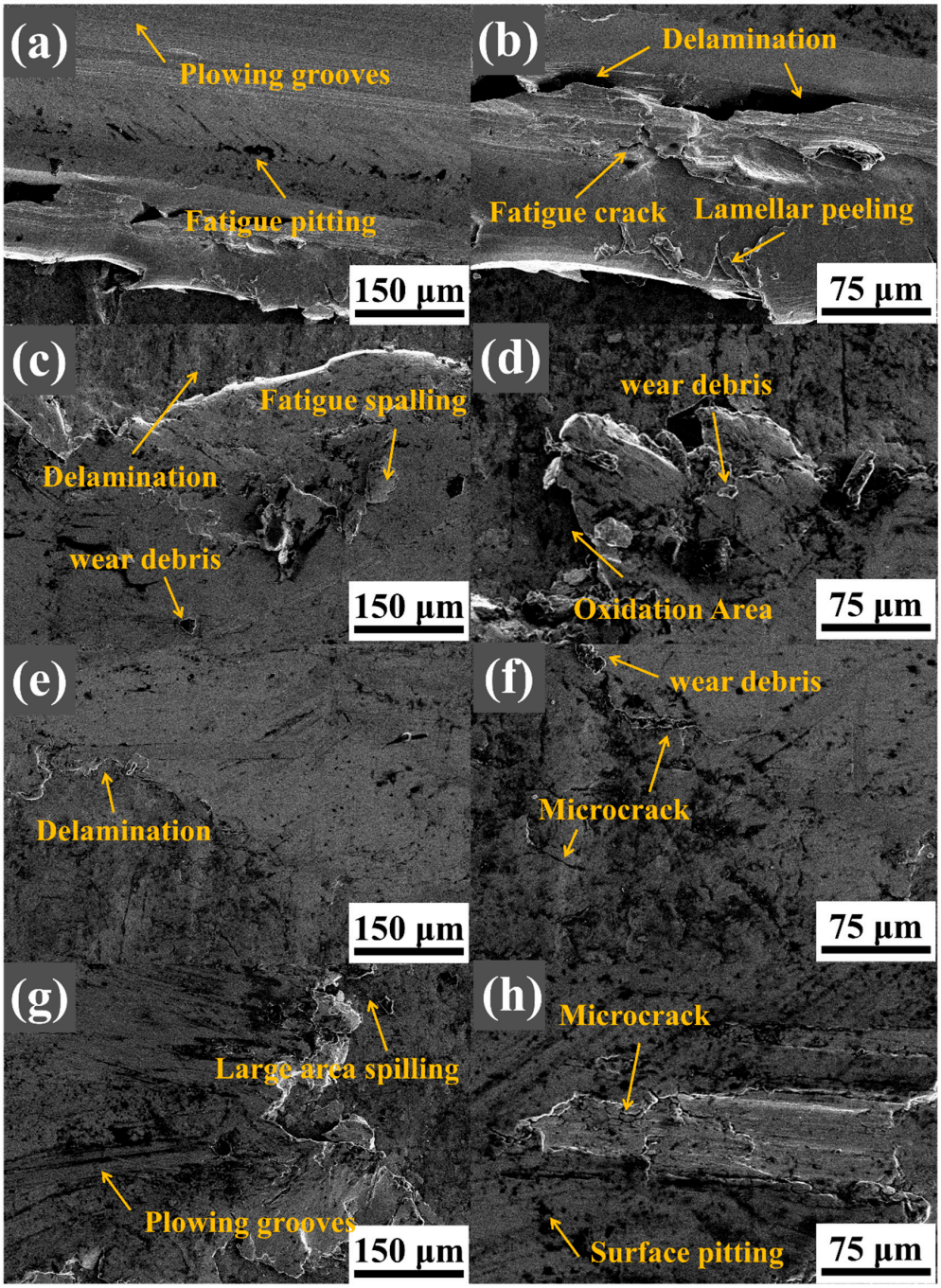

Figure 8. SEM images of wear scars tested under a load of 50 N and low magnification: (**a**) unMHP; (**c**) MHP-1.7; (**e**) MHP-2.7 and (**g**) MHP-3.5; and high magnification: (**b**) unMHP; (**d**) MHP-1.7; (**f**) MHP-2.7; and (**h**) MHP-3.5.

The unMHP exhibited severe composite wear characteristics with the most significant damage. Figure 8a shows prominent plowing grooves and fatigue pitting, indicating the simultaneous occurrence of abrasive and fatigue wear. Figure 8b reveals more complex damage patterns: lamellar peeling reflecting intense surface plastic deformation; fatigue cracks indicating cyclic loading-induced damage; and delamination resulting from the propagation and coalescence of surface and subsurface fatigue cracks. This synergistic effect of multiple wear mechanisms primarily stems from the untreated material's relatively low surface hardness and fatigue resistance, leading to adhesion/peeling cycles during reciprocating friction and ultimately resulting in severe material loss. MHP-1.7 demonstrated notably mitigated surface damage, characterized by combined fatigue and oxidative wear. Figure 8c shows fatigue spalling and localized delamination, indicating persistent but significantly reduced fatigue damage compared to unMHP in both distribution and depth. Figure 8d reveals oxidation areas and wear debris, suggesting mild oxidative and abrasive wear. This improved damage pattern can be attributed to surface strengthening effects induced by machine hammering, enhancing both plastic deformation resistance and fatigue life. MHP-2.7 exhibited optimal wear resistance, predominantly displaying mild fatigue wear characteristics. Figure 8e shows only minimal surface delamination, indicating excellent surface integrity. The presence of limited microcracks and wear debris in Figure 8f suggests moderate fatigue damage processes. This remarkable performance enhancement can be attributed to several synergistic mechanisms: (i) formation of an optimal work-hardened layer significantly improving plastic deformation resistance, (ii) induced compressive stress fields effectively suppressing fatigue crack initiation and propagation, and (iii) refined surface microstructure enhancing overall wear resistance. MHP-3.5 reverted to severe composite wear characteristics. Figure 8g shows large-area spalling and plowing grooves, indicating significant adhesive and abrasive wear. The surface pitting and microcracks in Figure 8h reflect severe fatigue damage. This performance degradation suggests excessive hammering energy led to surface over-deformation and structural damage, potentially through excessive work hardening-induced embrittlement, increased surface microstructural heterogeneity, and deterioration of residual stress distribution.

The microscopic morphological analysis systematically reveals the regulatory mechanism of hammering energy on CuSn12's surface damage behavior. At the optimal hammering energy of 2.7 J, the material achieved a transition from severe composite wear to mild single-fatigue wear, exhibiting superior wear resistance. These findings not only advance our understanding of hammering strengthening mechanisms but also provide microscopic-level scientific evidence for process parameter optimization. Future studies could incorporate in situ observation and multi-scale characterization techniques to establish a more comprehensive understanding of damage evolution mechanisms.

3.4. Electrochemical Corrosion

Electrochemical impedance spectroscopy (EIS) enables the characterization of interfacial properties, resistance, and capacitance of the electrolyte-passive film equivalent electrochemical system [40]. Figure 9a–c present the Nyquist plots, Bode modulus plots, and Bode phase angle diagrams obtained from measurements in 3.5 wt.% NaCl solution under open circuit potential (OCP) conditions for both the pristine and impacted specimens. Figure 9d illustrates the equivalent circuit model utilized for electrochemical analysis.

The Nyquist plots (Figure 9a) demonstrate that all impact-treated specimens exhibited larger capacitive arc diameters compared to the pristine sample, with the MHP-3.5 specimen showing the maximum diameter. The capacitive arc, which correlates to the double-layer capacitance and passive film capacitance, indicates that the pristine specimen's passive film

provided minimal protective characteristics to the substrate. In contrast, the passive films formed on impact-treated specimens offered enhanced substrate protection, with optimal protective properties observed for the specimen treated at 3.5 J impact energy.

The Bode modulus plots (Figure 9b) revealed a linear relationship between impedance magnitude and frequency over a wide frequency domain. The MHP-3.5 specimen exhibited significantly higher absolute impedance values compared to the pristine sample, while the MHP-1.7 specimen showed comparable impedance values, and the MHP-2.7 specimen demonstrated marginally elevated impedance values. Moreover, the MHP-3.5 specimen manifested the highest absolute impedance magnitude. The Bode phase angle plots indicated a maximum phase angle of ~66° for the pristine specimen, suggesting the formation of a stable passive film. The MHP-3.5 specimen demonstrated an enhanced maximum phase angle of ~74°, with all impact-treated specimens exhibiting higher phase angles compared to the pristine sample, indicating improved passive film stability and enhanced corrosion resistance post-impact treatment. The MHP-2.7 and MHP-1.7 specimens exhibited maximum phase angles of ~72° and ~71°, respectively.

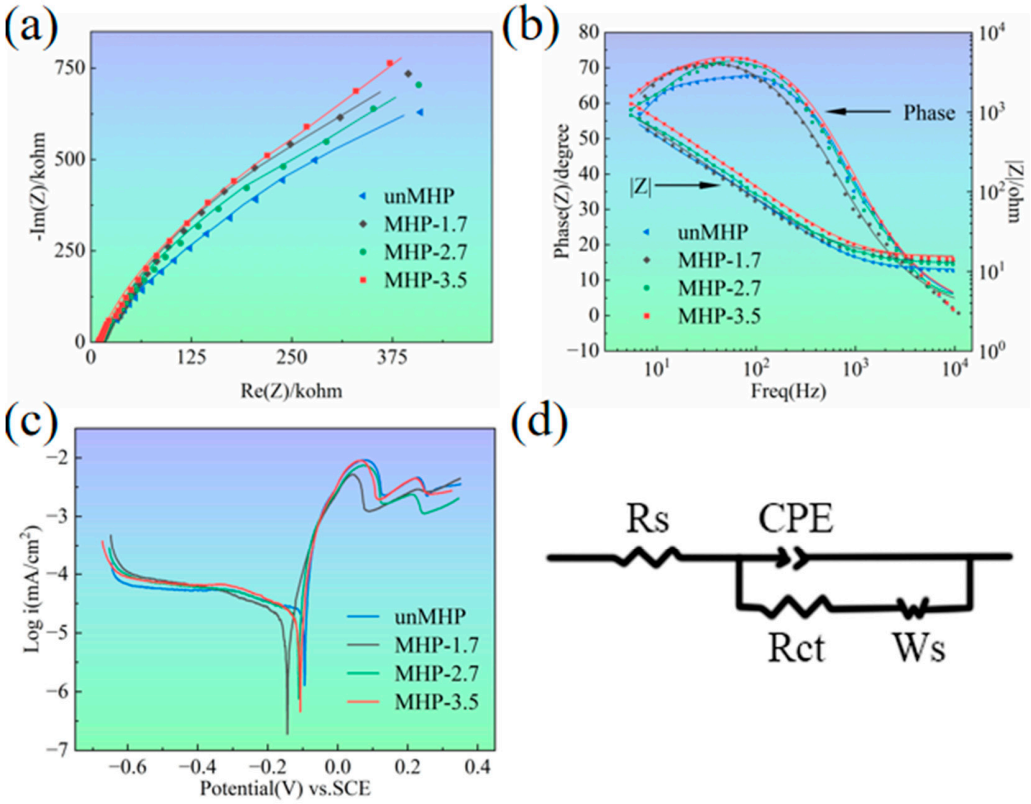

Figure 9. Electrochemical test analysis of different samples: (**a**) Nyquist diagram; (**b**) Bode diagram; (**c**) potentiodynamic polarization curves; and (**d**) equivalent circuit diagrams.

The potentiodynamic polarization curves (Tafel plots) shown in Figure 9c and their extrapolated parameters presented in Table 2 demonstrated the corrosion potential (E_{corr}) and corrosion current density (I_{corr}) for specimens treated at different impact energies. The data revealed that the MHP-3.5 specimen exhibited relatively noble corrosion potential and minimal corrosion current density. However, the pristine specimen demonstrated the most noble corrosion potential, while the MHP-1.7 specimen showed the most active potential and highest corrosion current density, indicating inferior corrosion resistance.

Table 2. Fitting parameters of potentiodynamic polarization curves.

Sample	E_{corr} (V_{SCE})	I_{corr} (mA/cm^2)
unMHP	−0.0937	−4.6352
MHP-1.7	−0.1482	−4.7038
MHP-2.7	−0.1235	−4.6436
MHP-3.5	−0.1202	−4.6258

Extensive research has been conducted on the corrosion resistance of surface-modified metals. Based on their oxide film formation capability, alloys can be categorized into passive and active metallic materials [41]. For passive metals, enhanced corrosion resistance is primarily attributed to the formation of passive films. The passive film formed on the specimen surface results in more noble corrosion potentials and lower corrosion current densities, thereby enhancing the metal's corrosion resistance. Conversely, while active metals exhibit increased grain boundary density and surface activity post-treatment, their corrosion resistance decreases due to the formation of unstable oxide films [42].

CuSn12, a passive metal, spontaneously forms a dense oxide film upon atmospheric exposure. In corrosive media containing aggressive anions, regions where passive film breakdown occurs without sufficient repassivation kinetics are susceptible to pitting corrosion [43]. Impact-treated specimens demonstrated enhanced corrosion resistance due to increased surface activity induced by microstructural defects (dislocations and twins) from plastic deformation. The MHP-3.5 specimen exhibited superior corrosion resistance, attributed to enhanced grain refinement and increased grain boundary density, facilitating rapid passive film formation and providing improved resistance against NaCl solution. However, compared to the pristine specimen, the MHP-1.7 specimen showed marginally lower corrosion resistance, likely due to preferential pitting at regions of lower activity resulting from heterogeneous plastic deformation.

Although mechanical impact treatment compromised surface uniformity through pit formation and increased surface roughness relative to the pristine specimen, the beneficial effects of induced defects and grain refinement superseded the detrimental impact of surface roughening, resulting in net improvement of corrosion resistance.

4. Conclusions

In this study, CuSn12 alloys were subjected to MHP with three different impact energies (1.7 J, 2.7 J, and 3.5 J), and the effects of impact energy on surface morphology, mechanical properties, and electrochemical properties were systematically investigated. The results showed that the influence of MHP treatment energy on surface morphology exhibited a non-monotonic trend, which differs from conventional shot peening technology. When the impact energy increased from 1.7 J to 2.7 J, both surface height difference and roughness decreased, and this anomalous phenomenon was attributed to strain hardening induced by increased dislocation density. Regarding mechanical properties, the microhardness of hammered specimens decreased systematically with increasing depth from the surface, with the 3.5 J impact energy treatment achieving the highest surface hardness of approximately 150 HV, representing a 40% increase compared to the untreated specimen. Wear resistance tests revealed that the 2.7 J impact energy treatment yielded optimal results, with an 82.7% reduction in volume wear loss and a stable friction coefficient of 0.45, while the wear mode transformed from severe composite wear to mild fatigue wear. In terms of corrosion resistance, as the impact energy increased from 2.7 J to 3.5 J, the material's corrosion resistance continuously improved, primarily due to grain refinement and the formation of surface passive films. However, the 1.7 J impact energy treatment reduced corrosion resistance due to the formation of pitting holes caused by non-uniform plas-

tic deformation. The results demonstrate that optimizing MHP process parameters can effectively enhance the comprehensive properties of CuSn12 alloy.

Author Contributions: Conceptualization, N.N. and L.Y.; methodology, S.X. and Q.T.; software, N.N. and S.X.; validation, L.Y., S.X. and C.D.; formal analysis, L.S. and H.W.; investigation, L.Y.; resources, Q.T. and C.D.; data curation, N.N., Q.T. and H.W.; writing—original draft preparation, L.S.; writing—review and editing, N.N and H.W.; visualization, L.Y. and C.D.; supervision, L.S. and H.W. All authors have read and agreed to the published version of the manuscript.

Funding: The research was supported by the Postgraduate Research & Practice Innovation Program of Jiangsu Province (KYCX24_3554), the Large Instruments Open Foundation of Nantong University (KFJN2428).

Data Availability Statement: The original contributions presented in this study are included in the article. Further inquiries can be directed to the corresponding authors.

Conflicts of Interest: No conflict of interest exists in the submission of this manuscript, and the manuscript was approved for publication by all authors.

References

1. Demirsöz, R. Wear behavior of bronze vs. 100Cr6 friction pairs under different lubrication conditions for bearing applications. *Lubricants* **2022**, *10*, 212. [CrossRef]
2. Zhao, L.; Li, J.; Yang, Q.; Wang, Y.; Zhang, X.; Li, H.; Yang, Z.; Xu, D.; Liu, J. Study on friction and wear properties of new self-lubricating bearing materials. *Crystals* **2022**, *12*, 834. [CrossRef]
3. Francis, R. *Copper Alloys in Seawater: Avoidance of Corrosion*; Copper Development Association: McLean, VA, USA, 2016.
4. Haq, M.I.U.; Raina, A.; Vohra, K.; Kumar, R.; Anand, A. An assessment of tribological characteristics of different materials under sea water environment. *Mater. Today Proc.* **2018**, *5*, 3602–3609. [CrossRef]
5. Babu, M.; Krishna, A.R.; Suman, K. Review of journal bearing materials and current trends. *Am. J. Mater. Sci. Technol.* **2015**, *4*, 72–83. [CrossRef]
6. Shifler, D.A. Understanding material interactions in marine environments to promote extended structural life. *Corros. Sci.* **2005**, *47*, 2335–2352. [CrossRef]
7. Sharif, K.; Evans, H.; Snidle, R. Prediction of the wear pattern in worm gears. *Wear* **2006**, *261*, 666–673. [CrossRef]
8. Sharif, K.; Evans, H.P.; Snidle, R.W.; Barnett, D.; Egorov, I.M. Effect of elastohydrodynamic film thickness on a wear model for worm gears. *Proc. Inst. Mech. Eng. Part J. J. Eng. Tribol.* **2006**, *220*, 295–306. [CrossRef]
9. Tekeli, S. Enhancement of fatigue strength of SAE 9245 steel by shot peening. *Mater. Lett.* **2002**, *57*, 604–608. [CrossRef]
10. Jia, M.; Wang, Y.; Yue, J.; Cao, C.; Li, K.; Yu, Y.; Li, Y.; Lu, Z. Recent progress in laser shock peening: Mechanism, laser systems and development prospects. *Surf. Interfaces* **2024**, *44*, 103757. [CrossRef]
11. Soyama, H. Cavitation peening: A review. *Metals* **2020**, *10*, 270. [CrossRef]
12. Huang, H.; Niu, J.; Xing, X.; Lin, Q.; Chen, H.; Qiao, Y. Effects of the shot peening process on corrosion resistance of aluminum alloy: A review. *Coatings* **2022**, *12*, 629. [CrossRef]
13. Ming, T.; Peng, Q.; Han, Y.; Zhang, T. Effect of water jet cavitation peening on electrochemical corrosion behavior of nickel-based alloy 600 in NaCl solution. *Mater. Chem. Phys.* **2023**, *295*, 127122. [CrossRef]
14. Soyama, H. Comparison between the improvements made to the fatigue strength of stainless steel by cavitation peening, water jet peening, shot peening and laser peening. *J. Mater. Process. Technol.* **2019**, *269*, 65–78. [CrossRef]
15. Jia, Y.; Cai, Z.; Yuan, M.; Wang, S.; Ma, L. Influence of shot-peening treatment on wear resistance of medium manganese steel. *J. Mater. Res. Technol.* **2024**, *31*, 3703–3711. [CrossRef]
16. Li, X.; Zhou, L.; Zhao, T.; Pan, X.; Liu, P. Research on wear resistance of AISI 9310 steel with micro-laser shock peening. *Metals* **2022**, *12*, 2157. [CrossRef]
17. Cho, K.T.; Song, K.; Oh, S.H.; Lee, Y.-K.; Lim, K.M.; Lee, W.B. Surface hardening of aluminum alloy by shot peening treatment with Zn based ball. *Mater. Sci. Eng. A* **2012**, *543*, 44–49. [CrossRef]
18. Kikuchi, S.; Nakamura, Y.; Nambu, K.; Ando, M. Effect of shot peening using ultra-fine particles on fatigue properties of 5056 aluminum alloy under rotating bending. *Mater. Sci. Eng. A* **2016**, *652*, 279–286. [CrossRef]
19. Valiev, R.Z.; Estrin, Y.; Horita, Z.; Langdon, T.G.; Zehetbauer, M.J.; Zhu, Y. Producing bulk ultrafine-grained materials by severe plastic deformation: Ten years later. *JOM* **2016**, *68*, 1216–1226. [CrossRef]
20. Niu, J.; Liu, Z.; Wang, G.; Huang, W.; Xu, Y. Anticorrosion property enhancement of Al–Li alloy 2A97 by lowering machined surface roughness. *Mater. Corros.* **2020**, *71*, 1980–1988. [CrossRef]

21. Wu, Y.; Kang, Y.; Chen, Y. Effect of shot peening on the corrosion and wear resistance of 2205 duplex stainless steel. *J. Mater. Eng. Perform.* **2023**, *32*, 3186–3201. [CrossRef]
22. Lv, Y.; Zhao, B.; Zhang, H.; Su, C.; Nie, B.; Wang, R.; Cao, L.; Lyu, F. Improving corrosion resistance properties of nickel-aluminum bronze (NAB) alloys via shot peening treatment. *Mater. Trans.* **2019**, *60*, 1629–1637. [CrossRef]
23. Niu, J.; Liu, Z.; Qiao, Y.; Wang, X.; Chen, H. Novel combination of indicators to compare the corrosion behaviors of Al, Al–Li alloy 2A97, and other Al alloys. *Mater. Corros.* **2022**, *73*, 171–179. [CrossRef]
24. Deng, Y.; Liu, J.; Qiao, Y.; Niu, J. Comparative investigations on the electrochemical behaviors among Al and aluminum alloys. *Mater. Res. Express* **2020**, *7*, 116510. [CrossRef]
25. Tang, W.; Li, S.; Huang, Y.; Ming, H.; Wang, X.; Li, L.; Wang, X.; Liu, Z. Surface strengthening mechanisms of laser shock peening additive manufacturing CuSn alloys: Experimental and numerical simulation investigations. *Surf. Coat. Technol.* **2025**, *495*, 131567. [CrossRef]
26. Li, X.; Wang, X.; Chen, B.; Gao, M.; Jiang, C.; Yuan, H.; Zhang, X.; Liang, T. Effect of ultrasonic surface rolling process on the surface properties of CuCr alloy. *Vacuum* **2023**, *209*, 111819. [CrossRef]
27. Revilla-Gomez, C.; Buffiere, J.-Y.; Verdu, C.; Peyrac, C.; Daflon, L.; Lefebvre, F. Assessment of the surface hardening effects from hammer peening on high strength steel. *Procedia Eng.* **2013**, *66*, 150–160. [CrossRef]
28. Curtat, J.-L.; Lanteigne, J.; Champliaud, H.; Liu, Z.; Lévesque, J.-B. Influence of hammer peening on fatigue life of E309L steel used for 13% Cr-4% Ni blade runner repairs. *Int. J. Fatigue* **2017**, *100*, 68–77. [CrossRef]
29. Liu, C.W.; Liao, K.; Chen, J.W. Simulation and Experimental Study on Effect of Shot Peening on Surface Roughness of 7075-T651 Aluminum Alloy. *Trans. Mater. Heat Treat.* **2021**, *42*, 172–180. (In Chinese) [CrossRef]
30. Bhat, K.U.; Panemangalore, D.B.; Kuruveri, S.B.; John, M.; Menezes, P.L. Surface modification of 6xxx Series aluminum alloys. *Coatings* **2022**, *12*, 180. [CrossRef]
31. Wang, H.; Ning, C.; Huang, Y.; Cao, Z.; Chen, X.; Zhang, W. Improvement of abrasion resistance in artificial seawater and corrosion resistance in NaCl solution of 7075 aluminum alloy processed by laser shock peening. *Opt. Lasers Eng.* **2017**, *90*, 179–185. [CrossRef]
32. Lei, C.; Chen, X.; Li, Y.; Chen, Y.; Yang, B. Enhanced corrosion resistance of SA106B low-carbon steel fabricated by rotationally accelerated shot peening. *Metals* **2019**, *9*, 872. [CrossRef]
33. Kumar, P.; Mahobia, G.; Mandal, S.; Singh, V.; Chattopadhyay, K. Enhanced corrosion resistance of the surface modified Ti-13Nb-13Zr alloy by ultrasonic shot peening. *Corros. Sci.* **2021**, *189*, 109597. [CrossRef]
34. Hadzima, B.; Bukovina, M.; Dolezal, P. Shot peening influence on corrosion resistance of AE21 magnesium alloy. *Mater. Eng.* **2010**, *17*, 14–19.
35. Mhaede, M. Influence of surface treatments on surface layer properties, fatigue and corrosion fatigue performance of AA7075 T73. *Mater. Des.* **2012**, *41*, 61–66. [CrossRef]
36. Huttunen-Saarivirta, E.; Kilpi, L.; Pasanen, A.; Salminen, T.; Ronkainen, H. Tribocorrosion behaviour of tin bronze CuSn12 under a sliding motion in NaCl containing environment: Contact to inert vs. reactive counterbody. *Tribol. Int.* **2020**, *151*, 106389. [CrossRef]
37. Fontanari, V.; Benedetti, M.; Girardi, C.; Giordanino, L. Investigation of the lubricated wear behavior of ductile cast iron and quenched and tempered alloy steel for possible use in worm gearing. *Wear* **2016**, *350*, 68–73. [CrossRef]
38. Savaşkan, T.; Azaklı, Z. An investigation of lubricated friction and wear properties of Zn–40Al–2Cu–2Si alloy in comparison with SAE 65 bearing bronze. *Wear* **2008**, *264*, 920–928. [CrossRef]
39. Ünlü, B.S.; Atik, E. Evaluation of effect of alloy elements in copper based CuSn10 and CuZn30 bearings on tribological and mechanical properties. *J. Alloys Compd.* **2010**, *489*, 262–268. [CrossRef]
40. Chang, B.-Y.; Park, S.-M. Electrochemical impedance spectroscopy. *Annu. Rev. Anal. Chem.* **2010**, *3*, 207–229. [CrossRef]
41. Lei, J.; Wenfang, C.; Xiu, S.; Guang, L.; Lian, Z. Surface Nanocrystalline Characteristics and Corrostion Resistance of beta-Type Titanium Alloy. *Rare Met. Mater. Eng.* **2014**, *43*, 80–84. [CrossRef]
42. Patel, V.; Li, W.; Andersson, J.; Li, N. Enhancing grain refinement and corrosion behavior in AZ31B magnesium alloy via stationary shoulder friction stir processing. *J. Mater. Res. Technol.* **2022**, *17*, 3150–3156. [CrossRef]
43. Parangusan, H.; Bhadra, J.; Al-Thani, N. A review of passivity breakdown on metal surfaces: Influence of chloride-and sulfide-ion concentrations, temperature, and pH. *Emergent Mater.* **2021**, *4*, 1187–1203. [CrossRef]

Disclaimer/Publisher's Note: The statements, opinions and data contained in all publications are solely those of the individual author(s) and contributor(s) and not of MDPI and/or the editor(s). MDPI and/or the editor(s) disclaim responsibility for any injury to people or property resulting from any ideas, methods, instructions or products referred to in the content.